



# A Comparative Study of Deformation Behaviors Between Laser-Welded Joints and Base Metal of Ti-22Al-24.5Nb-0.5Mo Alloy

Zhenglong Lei, Heng Zhou, Yanbin Chen, Kezhao Zhang, and Bingwei Li

(Submitted November 12, 2018; in revised form April 5, 2019; published online July 25, 2019)

The tensile deformation behaviors of laser-welded Ti-22Al-24.5Nb-0.5Mo alloy joints have been investigated at room temperature and 650 °C using in situ tensile analysis methods. The  $\alpha_2$  phase had a significant influence on deformation behaviors of base metal at room temperature and 650 °C. The microcracks mainly nucleated in B2/ $\alpha_2$  phase boundaries or within  $\alpha_2$  phase and then propagated along B2/ $\alpha_2$  phase boundaries subsequently. Compared with the plastic fracture of base metal, the fracture modes of the fully B2-phase fusion zone at room temperature and 650 °C were quasi-cleavage and intergranular fracture, respectively. While dislocation slips became foremost deformation mode in the fusion zone at room temperature, there were a great amount of slip bands on the surface of grains caused by the slip systems. The microcracks of fusion zone at 650 °C nucleated and propagated along the grain boundaries of B2 phase. Owing to the lack of grain deformation, the cross-slip bands were in small quantities on the surface of B2 phase grains.

**Keywords** deformation behaviors, in situ analysis, laser welding, Ti<sub>2</sub>AlNb alloy

## 1. Introduction

Ti<sub>2</sub>AlNb-based alloys are widely used for manufacturing aerospace components due to their excellent high-temperature performance (Ref 1-3). The microstructures of Ti<sub>2</sub>AlNb-based alloys are generally composed of B2 phase (body-centered cubic structure), O phase (Ti:Al:Nb = 2:1:1, ordered orthorhombic structure),  $\alpha_2$  phase (hexagonal closed-packed structure) (Ref 4, 5). By now, most researches are focused on optimizing the microstructures and properties of Ti<sub>2</sub>AlNb-based alloys, and some meaningful progresses have been made in the past decades. A Ti-22Al-24.5Nb-0.5Mo alloy with excellent mechanical properties at room and elevated temperature would be used as the substitute for high-temperature Ni-based alloys (Ref 6, 7). While the major problem facing the engineering application of Ti<sub>2</sub>AlNb-based alloys is lack of reliable welding methods, a more-thorough research, which is related with welding process, is necessary.

Until now, the abundant researches on the microstructures and properties of Ti<sub>2</sub>AlNb-based alloys (Ref 8, 9) and, in particular, its weldability have been reported. Laser welding is applicable for joining Ti<sub>2</sub>AlNb-based alloys because of its high precision, efficiency, and flexibility. However, most researches on the laser welding process of Ti<sub>2</sub>AlNb-based alloys mainly involve optimizing the welding parameters and investigating

the microstructure–property relations of laser-welded joints. Lei et al. (Ref 10) has reported that the tensile ductility of laser-welded joints was decreased significantly compared with the base metal, while the microstructure of fusion zone for laser-welded joints was fully B2 phase. Wu et al. (Ref 11) and Chen et al. (Ref 12) have proved that phase composition of fusion zone, independent on the laser welding parameters, also was fully B2 phase. And the tensile strength and ductility were equal to that of the base metal. Wang et al. (Ref 13) have focused on bending properties and fracture behaviors for Ti<sub>2</sub>AlNb laser-welded joints, whose fracturing strain decreased with increasing laser heat input. But the researches on tensile deformation behaviors for laser-welded joints should be detailed discussion.

In summary, the tensile strengths of the laser-welded joints were comparable to base metal at room temperature and 650 °C. However, the plastic deformation abilities of the laser-welded joints were much lower than the base metal. This phenomenon was closely to the microstructural difference between the base metal and laser-welded joints, but very limited research has been conducted in this area. This study aims to investigate fracture mechanisms of the base metal and laser-welded joints of Ti<sub>2</sub>AlNb-based alloys using in situ tensile methods at room temperature and 650 °C. The initiating position and propagating path of cracks and their correspondence with microstructural characteristics are discussed in this paper.

## 2. Experimental

The Ti-22Al-24.5Nb-0.5Mo alloy sheets which chemical composition is (wt.%): Al, 9.3%; Nb, 38.16%; Mo, 0.9% with the balance being Ti, were used to fabricate the welded joints. The microstructures of the base metal are shown in Fig. 1. The black block phase, gray needle-like phase, and white matrix

Zhenglong Lei, Heng Zhou, Yanbin Chen, Kezhao Zhang, and Bingwei Li, State Key Laboratory of Advanced Welding and Joining, Harbin Institute of Technology, Harbin 150001, China. Contact e-mails: leizhenglong@hit.edu.cn and chenyb@hit.edu.cn.

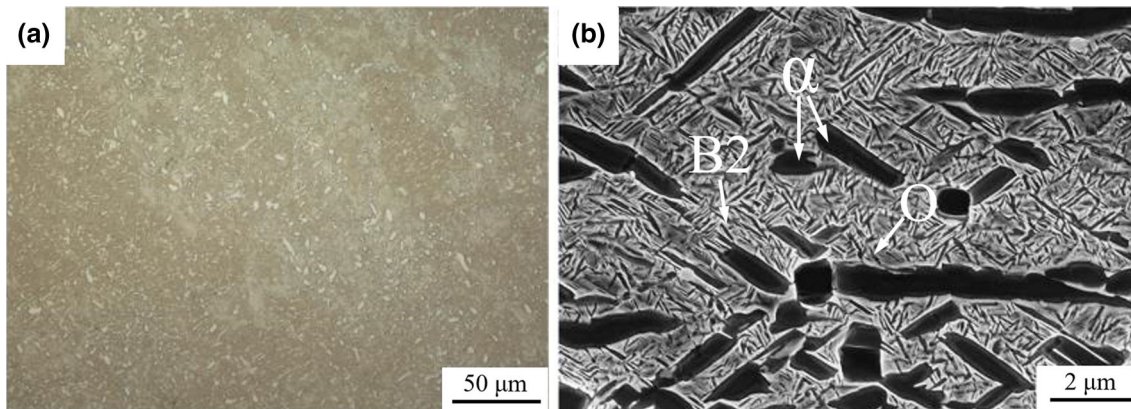


**Fig. 1** Microstructure of base metal: (a) overall microstructural characteristics and (b) a higher magnification of (a)

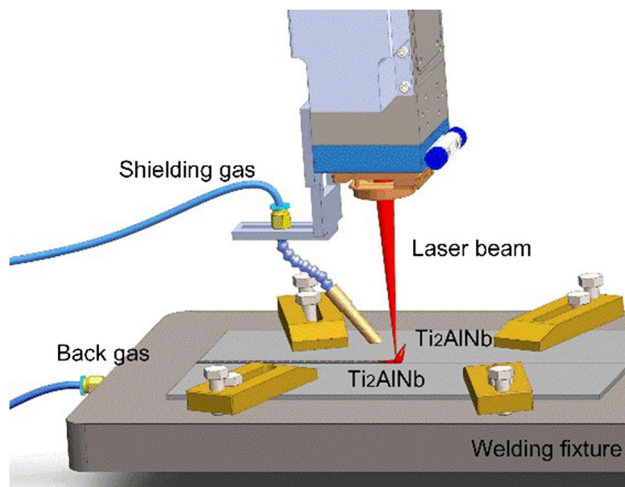


**Fig. 2** Schematic diagram of laser welding process

phases were  $\alpha_2$ , O, and B2 phases, respectively. The laser welding system was used by IPG YLS-5000 fiber laser (output wavelength of 1070 nm) and KUKA robot (accuracy of 0.1 mm). Laser welding process parameters were power 1000 W, welding speed 1 m/min, and defocus distance 0 mm. Argon was used as the shielding gas during welding process, and the gas flow of front and back shielding gas was 15 and 5 L/min, respectively. The schematic diagram is shown in Fig. 2.

The dimensions of specimens for in situ tensile testing at room temperature and 650 °C are shown in Fig. 3(a) and (b) respectively. In this paper, the main research focused on the fusion zone, because the fracture of laser-welded joints occurred at the fusion zone. Due to the low loading force of in situ tensile testing machine, the specimens were preset a notch at the center to allow cracks to propagate within the safe experimental load range. The preparations of the specimens for in situ tensile testing were similar to the metallographic samples. The specimens were cut using WEDM (wire electric discharge machine), followed by the use of 60 #, 1000 #, 2000 # diamond sandpaper to make its surface smooth. The specimens were polished by electrolytic polishing. The polishing solution was composed of methanol, *n*-butanol, and perchloric acid mixed solution (volume ratio of 6:3:1). The polishing parameters were polishing current 1A, voltage 20 V,

and time 90 s under liquid nitrogen cooling conditions. The polished samples were etched for 3-5 s using the Kroll reagent. The optical microscope used for microstructure observation was the VHX-1000E microscope of KEYENCE Company, with the maximum magnification factor of 1000. Phase analysis was performed using the D8 ADVANCE Da Vinci x-ray diffraction instrument from Germany.

In situ tensile test at room temperature was performed on the Quanta 200 scanning electron microscope (SEM) and the Microtest 2000N in situ tensile testing machine at a tensile rate of 0.05 mm/min. The tensile process was paused during the experiment to obtain a real-time SEM image. In situ tensile test at high temperature was performed on the high-temperature confocal laser scanning microscope (CLSM-HT). In order to protect the specimen against oxidized, the tensile process was performed in the argon atmosphere. The specimens were heated up to 650 °C and held for 5 min before loading. The real-time images were recorded at a rate of 15 fps. After fracture, the specimens were placed under scanning electron microscope (SEM) to observe the relationship between the deformability and the microstructures.

### 3. Results and Discussion

#### 3.1 Microstructure and Tensile Properties of the Welding Joints

As shown in Fig. 4, it was stable to obtain the excellent weld formation during the laser welding process of Ti-22Al-24.5Nb-0.5Mo alloy, which topside and backside surfaces of fusion zone were mildly sinking and protruding, respectively. The shape of the fusion zone was typical “Y-shaped,” because of unevenly distributed laser energy. In order to confirm the phase composition of the fusion zone, the XRD analysis testified that the fusion zone only contained B2 phase, as shown in Fig. 5. The results were consistent with the other researches of Ti<sub>2</sub>AlNb-based alloys’ welding (Ref 14, 15). The rapid cooling of the fusion zone from B2 phase zone, which inhibited the phase transformation from B2 phase to O and  $\alpha_2$  phases, resulted in the fully B2 phase (Ref 16).

Under the action of temperature, the microstructures had significant difference between the fusion zone and heat-affected zone (HAZ). According to the distance from fusion zone, HAZ was divided to near-HAZ and far-HAZ. This two zones

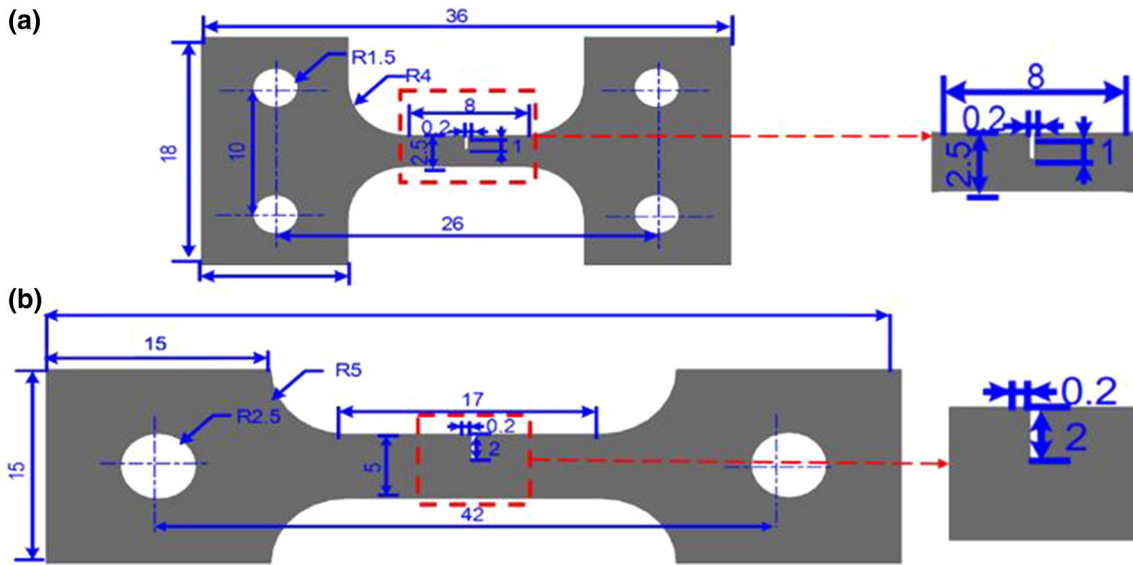


**Fig. 3** Geometric size of the tensile specimens for in situ observation at (a) room temperature and (b) 650 °C

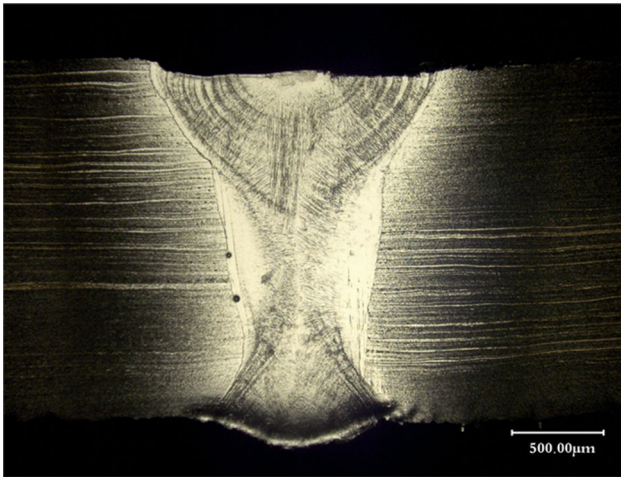


**Fig. 4** Cross-sectional morphology of the laser-welded joints of Ti-22Al-24.5Nb-0.5Mo

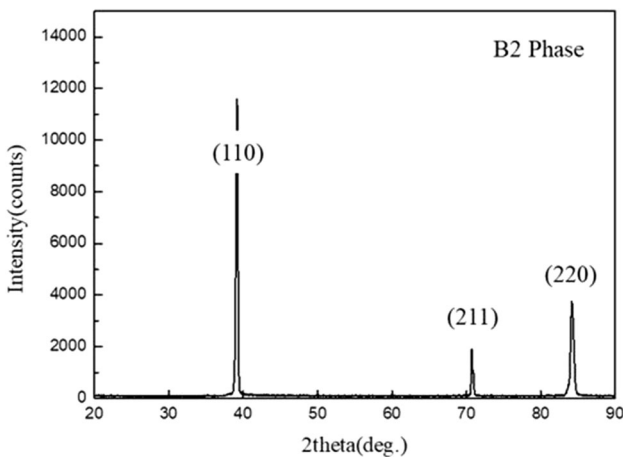


**Fig. 5** XRD analysis of the fusion zone of laser-welded joints

contained, respectively, B2 +  $\alpha_2$  phases and B2 + O +  $\alpha_2$  phases, as shown in Fig. 6. In far-HAZ, only part of O phase was dissolved in B2 matrix phase, as shown in Fig. 6(a). In near-HAZ, the O phase was all dissolved into B2 matrix phase, and the  $\alpha_2$  phase was partially dissolved in B2 matrix phase, as shown in Fig. 6(b).

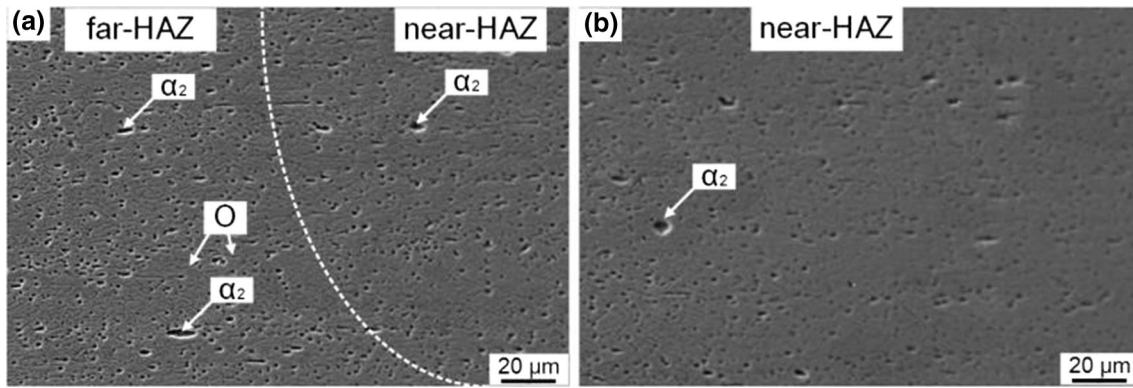
The large differences in tensile properties of base metal and laser-welded joints are distinctly shown in Fig. 7. It was obvious that the tensile strengths and elongations of base metal at room temperature and 650 °C were outstanding. The excellent tensile property of base metal benefited from compatibility of deformation for B2, O, and  $\alpha_2$  phases. Opposite to the properties of base metal, the laser-welded joints showed evident characteristics of brittle fracture. The elongation of welded joints at room temperature and 650 °C all were significantly decreased. The decreases in elongation were mainly affected by the microstructure of fully B2 phase in fusion zone.

Figure 8 shows the surfaces of fracture at room temperature and 650 °C. The fracture mode at room temperature was quasi-cleavage fracture as shown in Fig. 8(a), in which many river patterns existed on the fracture surface. The appearance of fracture at 650 °C showed that the joints fractured in the intergranular fracture mode, as shown in Fig. 8(b). The fractures of laser-welded joints at room temperature and 650 °C all occurred on the fusion zone. It was very significant to study the deformation behaviors of fusion zone. Based on the consequences of microstructures, the deformation behaviors of base metal and laser-welded joints of Ti-22Al-24.5Nb-0.5Mo would be expounded in sections 3.2 and 3.3.

### 3.2 Deformation Behaviors of Base Metal and Joints at Room Temperature

The in situ tensile results of Ti-22Al-24.5Nb-0.5Mo base metal are shown in Fig. 9. In the initial stage, no obvious change was observed in the microstructure of base metal, as shown in Fig. 9(a). During the loading process, the microcracks





**Fig. 6** Microstructures of heat-affected zone of laser-welded joints: (a) far-HAZ and near-HAZ (b) near-HAZ

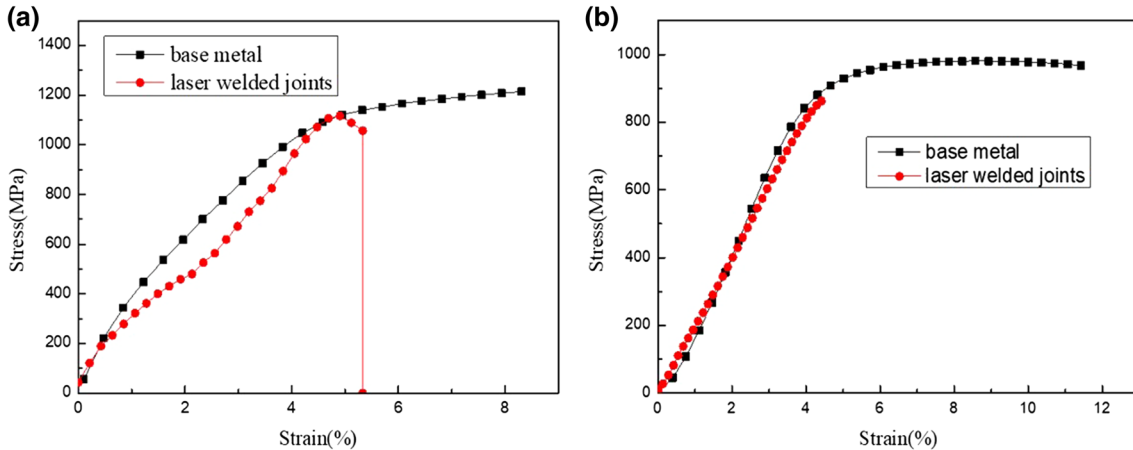


**Fig. 7** The tensile curve of the base metal and laser-welded joints at (a) room temperature and (b) 650 °C

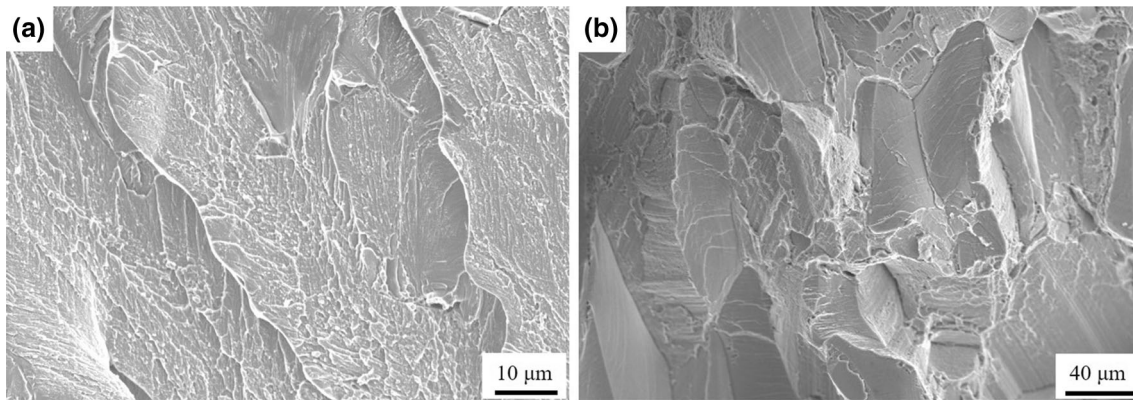


**Fig. 8** Appearances of fracture at room temperature and 650 °C: (a) room temperature, (b) 650 °C

were firstly generated within the  $\alpha_2$  phase grains, as shown in Fig. 9(b). With the increase in the tensile stress, microcracks also occurred along the B2/ $\alpha_2$  phase boundary, not only within the  $\alpha_2$  phase grains, which indicated the binding strength at the B2/ $\alpha_2$  phase boundary was higher than the strength of  $\alpha_2$  phase, as shown in Fig. 9(c). As the tensile process continued, the microcracks continued to expand until the tensile specimen failed, as shown in Fig. 9(d) and (e).

The results of in situ tensile testing for Ti-22Al-24.5Nb-0.5Mo joints are shown in Fig. 10. The stress loading direction was also perpendicular to the direction of the welding, as

shown in Fig. 10(a). In the initial stage, single-slip bands, cross-slip bands, and multiple slip bands occurred in different grains, as shown in Fig. 10(b). With the increase in the loading stress, the number of slip bands in the grains continued to increase. Meanwhile, due to the obstruction of the dislocation slip caused by the grain boundaries, there were some different slip directions within different grains, as shown in Fig. 10(c) and (d). As the loading process continued, the number of different slip bands also increased significantly. At the same time, the effects of grain boundaries on the dislocation slips were more obvious, which led to the plastic deformations on

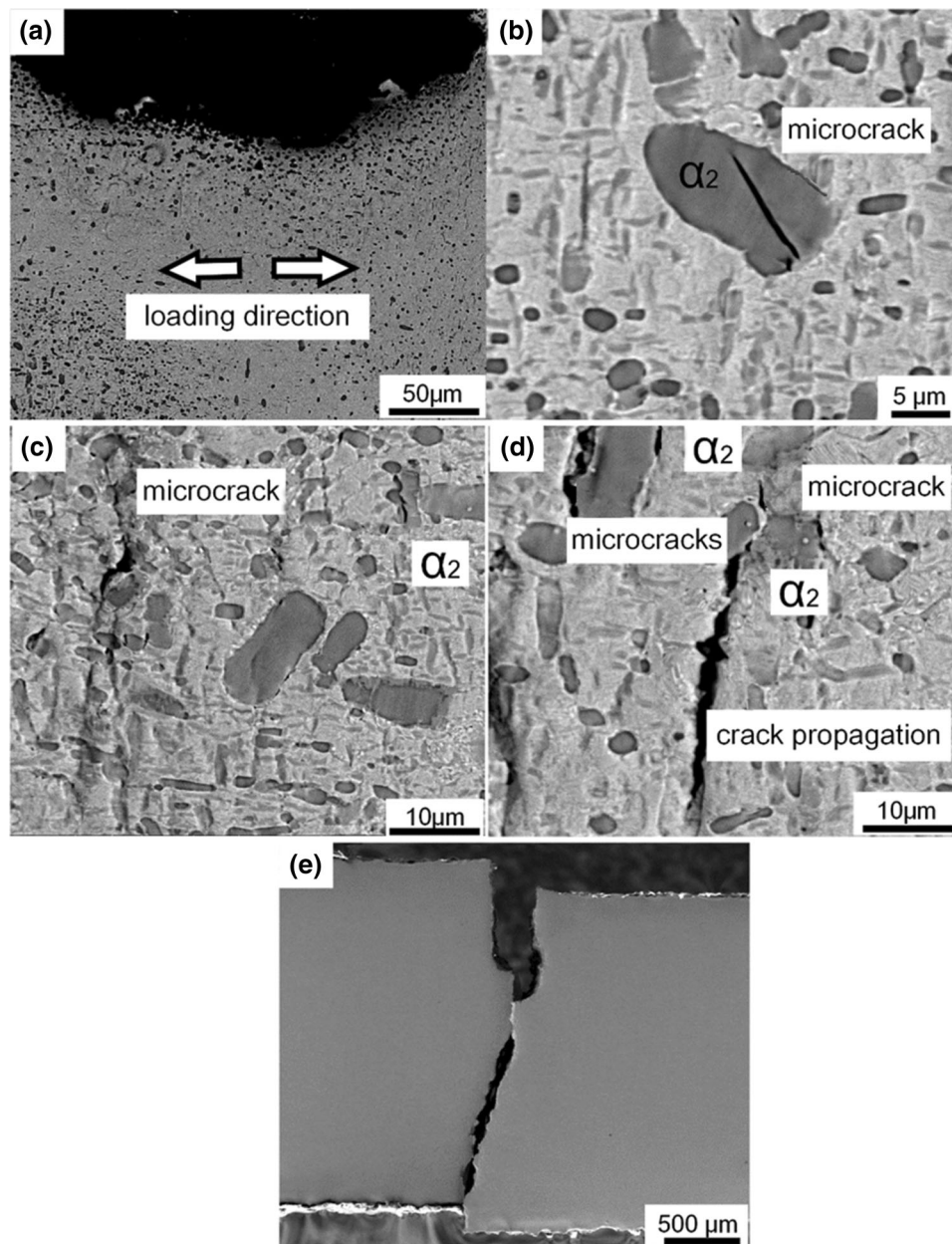


**Fig. 9** Results of in situ SEM analysis of base metal at room temperature: (a) loading direction, (b) microcracks within the  $\alpha_2$  phase, (c) microcracks along B2/ $\alpha_2$  phase boundaries, (d) crack propagation and (e) fracture in base metal

the grain boundaries were greater than the internal area of the grains, as shown in Fig. 10(e) and (f). As the deformations continued, the microcracks firstly appeared within the grains. And then the microcracks propagated and expanded, which eventually resulted in the fracture of the tensile specimens, as shown in Fig. 10(g) and (h).

The deformation behaviors of the base metal and laser-welded joints of Ti-22Al-24.5Nb-0.5Mo at room temperature were different from each other. The main difference focused on the locations of crack initiation and propagation paths. The base metal contains B2 phase,  $\alpha_2$  phase, and O phase, and the structures of the three phases are quite different. The  $\alpha_2$  phase was hexagonal close-packed structure with less slip systems when it was stressed. Only  $\langle a \rangle$  dislocations could be activated at room temperature, and therefore, the  $\alpha_2$  phase usually worked as a brittle phase (Ref 17, 18). Compared with  $\alpha_2$  phase, the

dislocation type of O phase that could be activated at room temperature was the  $\langle c + a/2 \rangle$  dislocation in addition to the  $\langle a \rangle$  dislocation. Therefore, O phase had better plastic deformation ability than the  $\alpha_2$  phase (Ref 19). Because B2 phase was a body-centered cubic structure, which had more slip systems, it was generally believed that B2 phase had the function of passivating cracks in the intermetallic compounds of titanium–aluminides. In the process of tensile deformation, the number of the dislocation within  $\alpha_2$  phase was less than the O phase, so it was difficult to relieve the stress concentration through the dislocation slip. Therefore, the microcracks initiation in  $\alpha_2$  phase was easier. As the stress continued to increase, the deformations between the  $\alpha_2$  phase and the B2 phase needed to be coordinated. The stress concentration would be caused at the phase interface, and the  $\alpha_2$  phase was not able to mitigate the stress concentration through the severe deformation. Therefore,



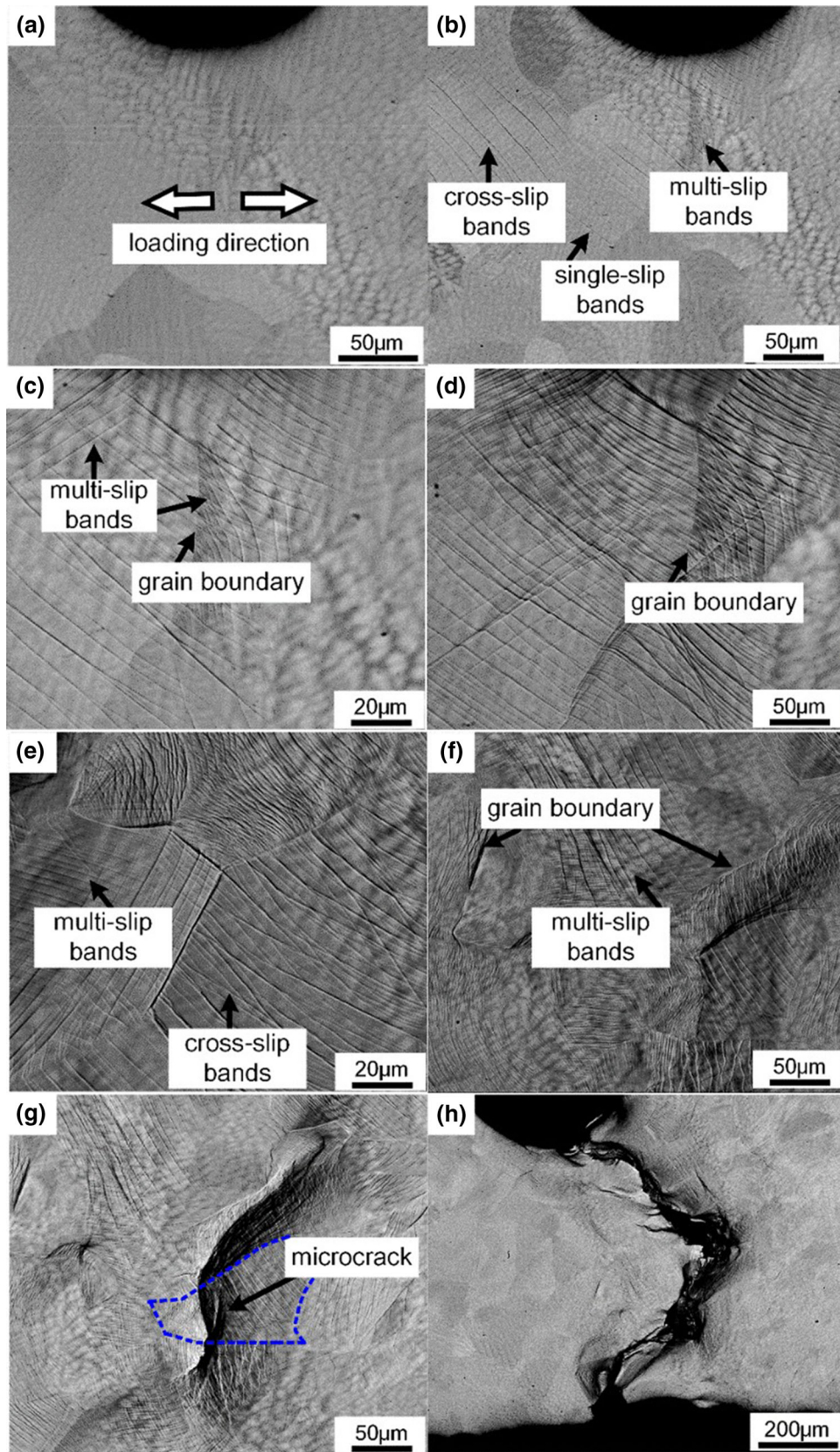


**Fig. 10** Results of in situ SEM analysis of welded joints at room temperature: (a) loading direction, (b) single-slip bands, cross-slip bands, and multi-slip bands, (c)-(f) multi-slip bands and grain boundary, (g) microcrack, (h) fracture in the fusion zone

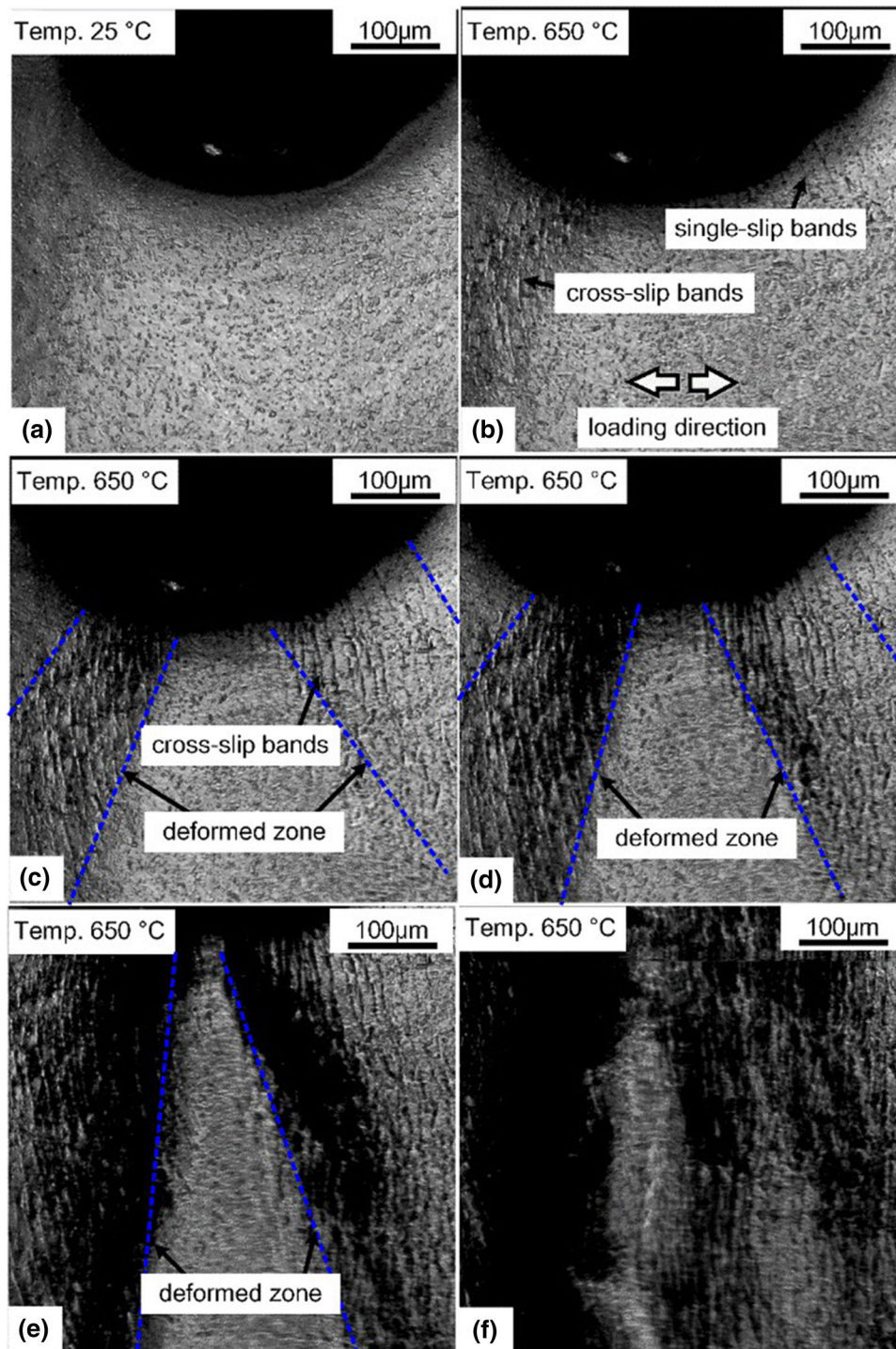


**Fig. 11** Results of in-SEM analysis of base metal at 650 °C: (a) unheated state, (b) single-slip bands and cross-slip bands at 650 °C, (c) cross-slip bands and deformed zone at 650 °C, (d), (e) microcracks formation of deformed zone at 650 °C, (f) fracture of base metal

the microcracks occurred on the  $\alpha_2$ /B2 phase boundary. However, the number of activated dislocation in O phase at room temperature was relatively larger. Thence, it also had good deformation coordination ability with B2 phase. No microcrack on O/B2 phase boundary was observed during the in situ tensile according to the above theory.

For the laser-welded joints of Ti-22Al-24.5Nb-0.5Mo alloy, the microstructure consisted of the fully B2 phase in coarse columnar morphology. Various slip bands (slip band, cross-slip

band, and multi-line slip band) could be observed during in situ tensile tests. Microcracks were mainly concentrated in the interior of B2 grains. This phenomenon was caused by the B2 phase which was body-centered cubic structure with good plasticity. Under stress, not only  $\{112\}$  twins but also dislocation slip could occur. The dislocation slip direction was  $[111]$ , and slip plane could be  $\{110\}$ ,  $\{112\}$ , and  $\{123\}$ . Therefore, only partial slip systems can be activated and slip band types were single slip when the stress was small. As the



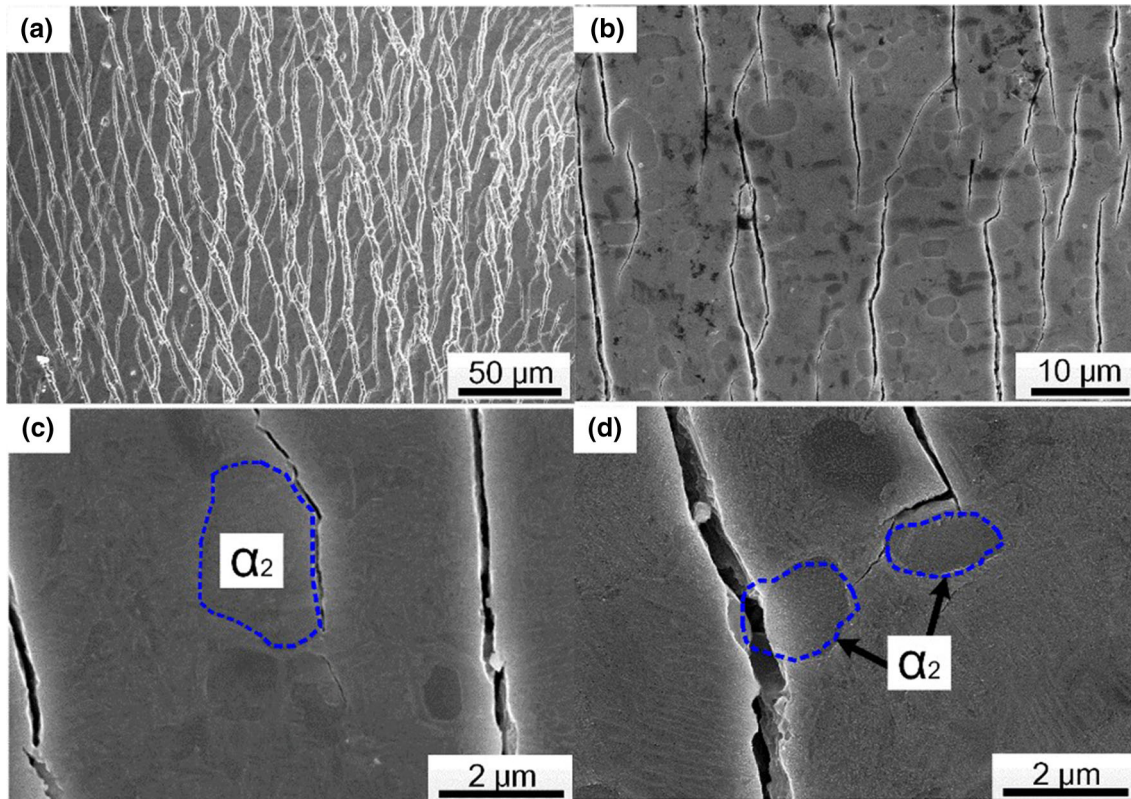


**Fig. 12** Morphology of the tensile specimen surface of base metal after in situ tests at 650 °C: (a) microcracks of base metal, (b) a higher magnification of (a), (c) microcrack initiation on the B2/ $\alpha_2$  phase boundary, (d) microcrack propagation in the  $\alpha_2$  phase

stress was increased further, the slip band type became cross-slip, which two or more different slip planes slipped along [111] crystal orientation. Since the grain boundary had high strength at room temperature, the critical shear stress of multiple slip systems satisfied Schmid's law when the stress was increased further. In this case, the type of slip band turned to multiple slips. As the amount of deformation increased, microcracks could initiate within the crystal. The slip of B2 phase mainly depended on the low-index crystal plane. After a large amount of deformation of B2 phase, these low-index crystal planes have slipped gradually cracked. After initiation of microcracks, the low-index free surface exposed was a close-packed surface of atoms with a small surface energy, and therefore, the crack cleaved along the crystal plane and eventually formed a fracture along the crystal plane.

### 3.3 Deformation Behaviors of Base Metal and Joints at 650 °C

The results of in situ tensile tests for Ti-22Al-24.5Nb-0.5Mo alloy at 650 °C are shown in Fig. 11. The microstructures are shown in Fig. 11(a) under heating. At 650 °C, a small amount of flat single-slip bands and cross-slip bands were formed near the notch, as shown in Fig. 11(b), which was the result of severe deformation near the notch. As the stress increased, the single-slip band in Fig. 11(b) converted gradually to the slip, and the original slip band gradually expanded toward the base metal to form a symmetrical deformation zone distributed near the notch, as shown in Fig. 11(c). As the tensile process proceeded, microcracks were preferentially formed near the notch due to the largest deformation, as shown in Fig. 11(d).

The continued microcracks could form macroscopic cracks and eventually led to the fracture of the tensile specimens, as shown in Fig. 11(e) and (f).

The morphology of the specimen surface of the base metal was observed under SEM, after the in situ tensile test at 650 °C. The relationships between microcrack initiation, propagation, and microstructure were further observed, as shown in Fig. 12. Extensive microcracks existed near the fracture surface of the tensile specimen, as shown in Fig. 12(a) and (b). In Fig. 12(c), the microcracks occurred on the  $\alpha_2$ /B2 phase boundary, which was the same as that of the microcracks initiation during the room temperature tensile deformation. This phenomenon showed that crack initiation was led by the mismatch between  $\alpha_2$  phase and B2 phase. During the propagation of microcracks, the tip of crack propagated from the B2 phase to the  $\alpha_2$  phase internally, and finally the crack broke through the inside of  $\alpha_2$  phase, as shown in Fig. 12(d).

The results of the in situ tensile at 650 °C for the laser-welded joints of the Ti-22Al-24.5Nb-0.5Mo alloy are shown in Fig. 13. Compared with the microstructure of the fusion zone at room temperature, the grain boundaries of B2 phase were more pronounced in heating processing, as shown in Fig. 13(a) and (b). At the beginning of the tensile process, the phenomenon that the single-slip zone located inside the B2 phase grains was first found near the notch, as shown in Fig. 13(c). When the stress was increased to a certain extent, the microcracks preferentially formed on the grain boundary of the B2 phase and then began to expand along the grain boundaries, as shown in Fig. 13(d). When the initially formed 2# microcracks propagated, the microcrack tip entered the interior of the Grain B. While its expansion path was obstructed by Grain B, a new



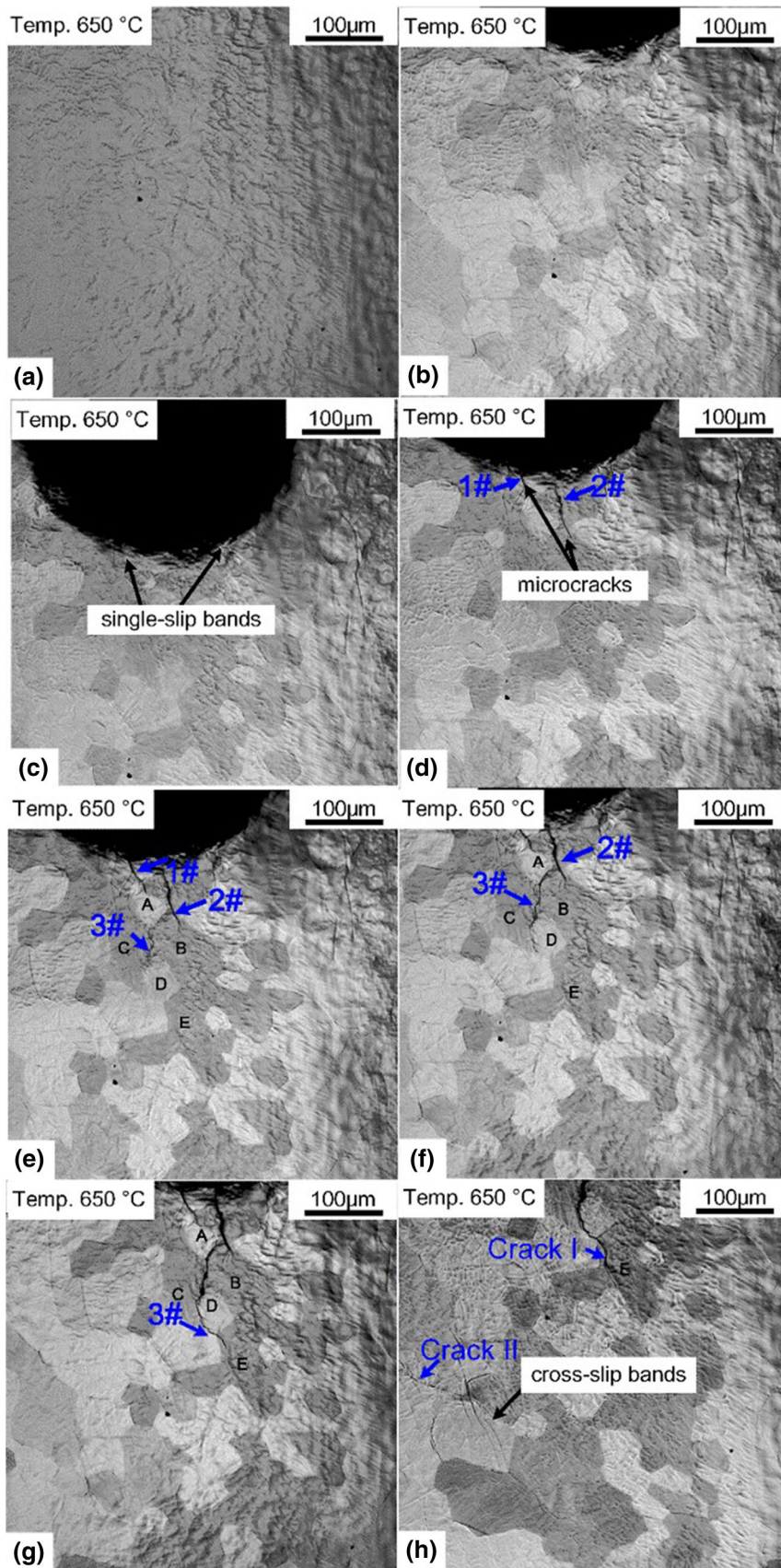


**Fig. 13** Results of in-SEM analysis of laser-welded joints at 650 °C: (a) insulation process at 650 °C, (b) loading at 650 °C, (c) slip bands at 650 °C, (d) microcrack initiated along the grain boundaries, (e), (f) microcrack propagation, (f) microcrack propagated into Grain E, (h) formation of Crack II

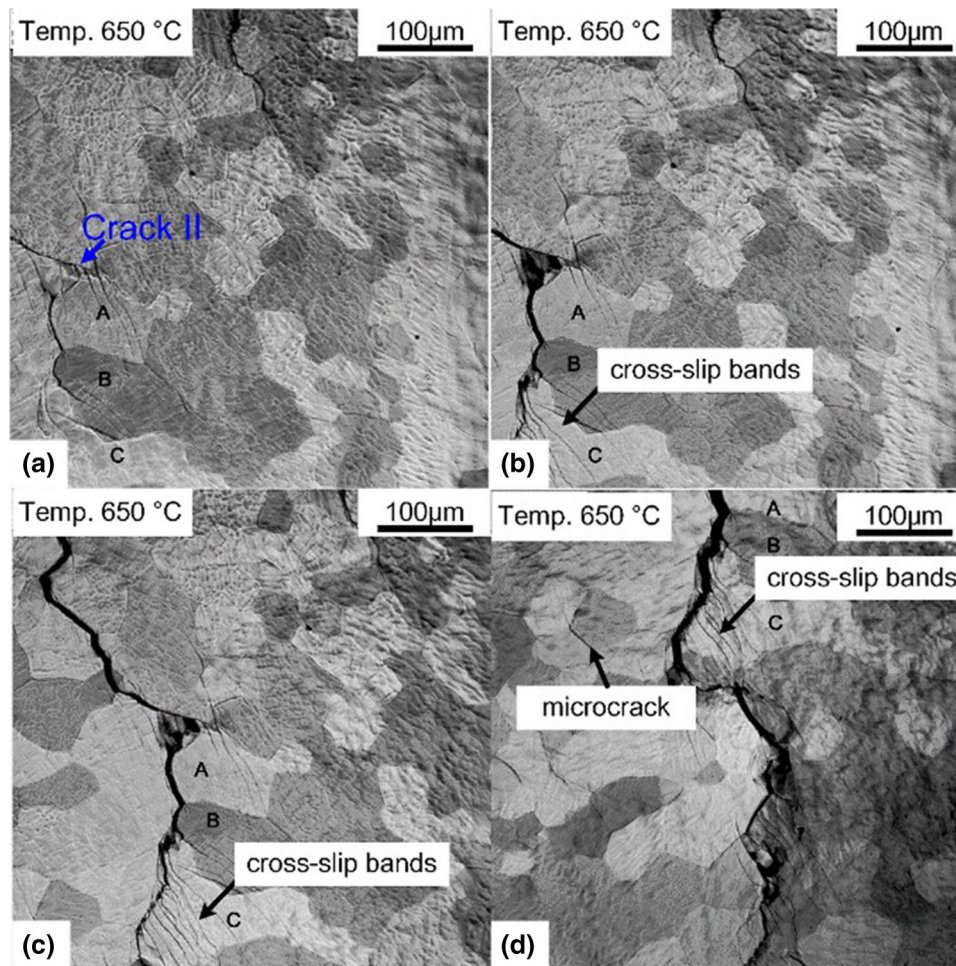


**Fig. 14** Crack propagation process of Crack II. (a)-(d) cracks along the B2 boundaries

3# microcrack formed on B/C grain boundary, as shown in Fig. 13(e), which indicated that the intragranular strength of the fully B2-phase was higher than the grain boundary strength during high-temperature tensile deformation. As the tensile process continued, the 3# microcrack propagated further along the A/B grain boundary and the C/D grain boundary, as shown in Fig. 13(f). When the 3# microcrack propagated along the C/D grain boundary to the inside of the grain E, the expansion path was also hindered by the Grain E. And then the microcrack stopped expanding within the Grain E. Because the extension was blocked, a new source of microcrack formed in the lower left area, which was defined as microcrack I and microcrack II, respectively, as shown in Fig. 13(g) and (h). The expansion of microcrack II is shown in Fig. 14. The expansion path was basically along the grain boundaries of grains A, B, and C, as shown in Fig. 14(a), (b), (c), and (d). At the same time, the microcrack formed in the slip zone was found in the grains A, B, and C. During the subsequent microcrack expansion, similar microcracks were found in the grains on the crack expansion path.

The specimen surface morphology of laser-welded Ti-22Al-24.5Nb-0.5Mo joints at 650 °C is shown in Fig. 15. Firstly, the main crack propagation path was not completely along the B2 phase boundary, as shown in Fig. 15(a). A number of microcracks could be observed near the main crack. It could be seen that the microcracks were mostly generated by

dislocation slipping, as shown in Fig. 15(b), (c), and (d). It could be seen that some microcracks intersected with each other and showed the features of cross-slip and multi-slip. The number of microcracks farther from the main crack was less.

Compared with the in situ tensile testing results of Ti-22Al-24.5Nb-0.5Mo alloy base metal at room temperature and 650 °C, the deformation process of the base metal was significantly affected by the coordination of the deformation of each phase. At both room temperature and 650 °C, the microcracks initiated and propagated mainly at the B2/ $\alpha_2$  phase boundary, which was close with the high-temperature fracture mode of the base metal. This was the results that the base metal was in a more stable equilibrium state, and the base metal maintained similar microstructures throughout the high temperature during the tensile process. For Ti-22Al-24.5Nb-0.5Mo laser-welded joints, there were significant differences in the in situ tensile process at room temperature and 650 °C. During the deformation process at room temperature, the deformation mainly depended on the multi-slip of dislocations due to the more slip systems of B2 phase. The fracture mode was transgranular cleavage fracture, which indicated that the grain boundary strength was higher than the intragranular intensity. However, at high temperature (650 °C), the crack propagation proceeded mainly along grain boundaries of the B2 phase. The slip zone inside the grain was dominated by a single cross-slip, indicating that the grain boundary strength was decreased at



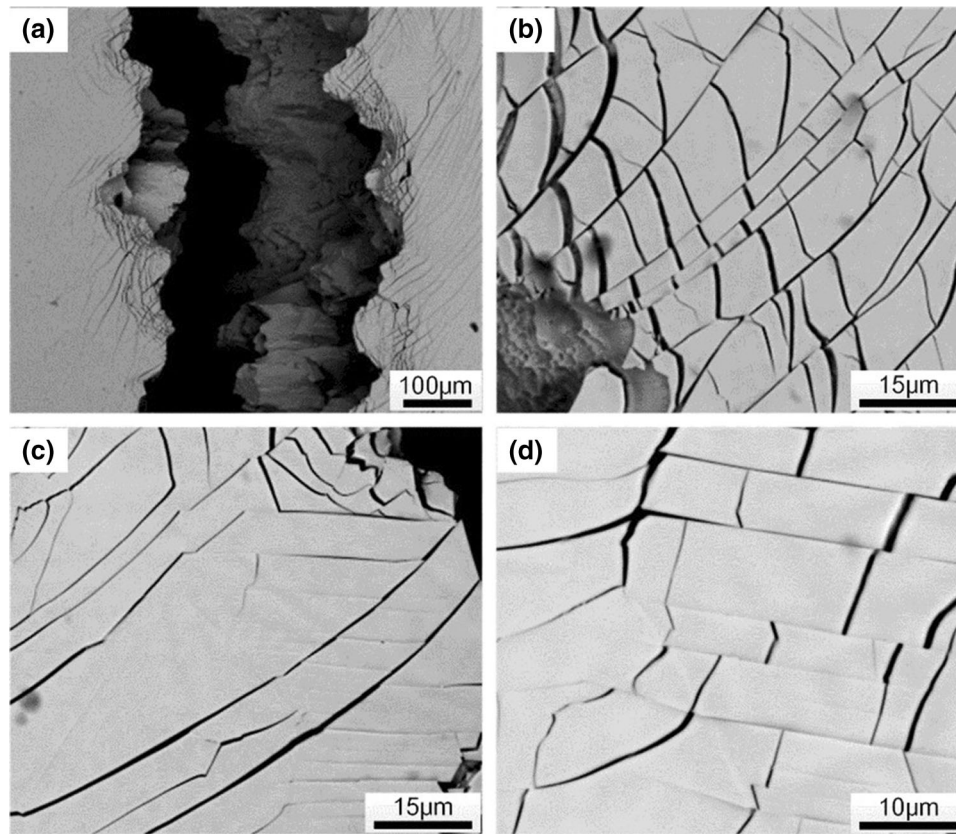


**Fig. 15** Morphology of the tensile specimen surface of the fusion zone of laser-welded Ti-22Al-24.5Nb-0.5Mo joints after in situ tests at 650 °C: (a) overall morphology, (b)-(d) microcracks and slip bands

high temperature. No severe plastic deformation occurred with the grains.

#### 4. Conclusion

The in situ tensile tests at room temperature and 650 °C of Ti-22Al-24.5Nb-0.5Mo alloy were performed on the base metal and the joints, respectively. The relationship between microstructure and deformation behavior was established.

- (1) The microstructure of laser-welded joints of Ti-22Al-24.5Nb-0.5Mo was fully B2 phase. Compared with the base metal, the deformation behaviors were mainly affected by the microstructures.
- (2) During the in situ tensile testing of the base metal at room temperature, the initiation and propagation of microcracks occurred within the  $\alpha_2$  phase and on the B2/ $\alpha_2$  phase interface.
- (3) The in situ tensile test of the welded joints at room temperature was characterized by single-slip zone, cross-slip zone, and multi-slip, and the fracture mode was transgranular cleavage fracture.
- (4) The microcracks of base metal at 650 °C only nucleated on the B2/ $\alpha_2$  phase interface and extend along the phase interface. The fracture of the welded joints at 650 °C was fractured along the grain boundary, and the internal slip of the grain was less.

#### Acknowledgment

This work is supported by the National Key R&D Program of China under Grant No. 2017YFB1301600 and Heilong Jiang Postdoctoral Funds for Scientific Research Initiation (LBH-Q15038).

#### References

1. R.R. Boyer, An Overview on the Use of Titanium in the Aerospace Industry, *Mater. Sci. Eng. A*, 1996, **213**(1-2), p 103-114
2. C. Veiga, J.P. Davim, and A.J.R. Loureiro, Properties and Applications of Titanium Alloys: A Brief Review, *Rev. Adv. Mater. Sci.*, 2012, **32**(2), p 134-148
3. A. Partridge and E.F.J. Shelton, Processing and Mechanical Property Studies of Orthorhombic Titanium-Aluminide-Based Alloys, *Air Space Eur.*, 2001, **2**(3-4), p 170-173
4. D. Banerjee, A.K. Gogia, T.K. Nandi et al., A New Ordered Orthorhombic Phase in a Ti<sub>3</sub>Al-Nb alloys, *Acta Metall.*, 1988, **36**(4), p 871-882
5. H.Z. Niu, Y.F. Chen, D.L. Zhang et al., Fabrication of a Powder Metallurgy Ti<sub>2</sub>AlNb-Based Alloy by Spark Plasma Sintering and Associated Microstructure Optimization, *Mater. Des.*, 2016, **89**, p 823-829
6. B. Chen, H. Xiong, B. Sun et al., Microstructure Evolution and Tensile Properties of Ti<sub>3</sub>Al/Ni-based Superalloy Welded Joint, *J. Mater. Sci. Technol.*, 2014, **30**(7), p 715-721
7. X. Jiao, G. Liu, D. Wang et al., Creep behavior and effects of heat treatment on creep resistance of Ti-22Al-24Nb-0.5Mo alloy, *Mater. Sci. Eng. A*, 2016, **680**, p 182-189
8. L. Germann, D. Banerjee, J.Y. Guédou et al., Effect of Composition on the Mechanical Properties of Newly Developed Ti<sub>2</sub>AlNb-Based Titanium Aluminide, *Intermetallics*, 2005, **13**(9), p 920-924

9. S. Emura, K. Tsuzaki, and K. Tsuchiya, Improvement of Room Temperature Ductility for Mo and Fe Modified Ti<sub>2</sub>AlNb Alloy, *Mater. Sci. Eng. A*, 2010, **528**(1), p 355-362
10. Z. Lei, Z. Dong, Y. Chen et al., Microstructure and Tensile Properties of Laser Beam Welded Ti-24Al-27Nb Alloys, *Mater. Des.*, 2013, **46**, p 151-156
11. A.P. Wu, G.S. Zou, J.L. Ren et al., Microstructure and Mechanical Properties of Ti-24Al-17Nb (at%) Laser Beam Welding Joints, *Intermetallics*, 2002, **10**(7), p 647-652
12. Y. Chen, K. Zhang, X. Hu et al., Study on Laser Welding of a Ti-22Al-25Nb Alloy: Microstructural Evolution and High Temperature Brittle Behavior, *J. Alloys Compd.*, 2016, **681**, p 175-185
13. G.Q. Wang, A.P. Wu, G.S. Zou et al., Bending Properties and Fracture Behavior of Ti-23Al-17Nb Alloy Laser Beam Welding Joints, *Tsinghua Sci. Technol.*, 2009, **14**, p 293-299
14. X. Liu, S. Wu, Y. Ji et al., Ultrasonic Frequency Pulse Tungsten Inert Gas Welding of Ti<sub>2</sub>AlNb-Based Alloy, *Chin. J. Rare Met.*, 2014, **38**, p 541
15. J.M. Yin, B. Lu, and Y.L. Li, Electron beam welding of Ti<sub>2</sub>AlNb based alloy sheet, *Chin. J. Nonferr. Met.*, 2010, **20**, p 325-330
16. J. Kumpfert and W.A. Kaysser, Orthorhombic Titanium Aluminides: Phases, Phase Transformations and Microstructure Evolution, *Z. Metall.*, 2001, **2001**(92), p 128-134
17. S. Jun and F. Aihan, Recent Advances on Microstructural Controlling and Hot Forming of Ti<sub>2</sub>AlNb-Based Alloys, *Acta Metall. Sin.*, 2013, **49**(11), p 1286-1294
18. J. Peng, Y. Mao, S. Li et al., Microstructure Controlling by Heat Treatment and Complex Processing for Ti<sub>2</sub>AlNb Based Alloys, *Mater. Sci. Eng. A*, 2001, **299**(1), p 75-80
19. T.K. Nandy and D. Banerjee, Deformation Mechanisms in the O Phase, *Intermetallics*, 2000, **8**(9), p 1269-1282

**Publisher's Note** Springer Nature remains neutral with regard to jurisdictional claims in published maps and institutional affiliations.